


Are pulsars born with a hidden magnetic field?

Alejandro Torres-Forné,¹ Pablo Cerdá-Durán,¹ José A. Pons² and José A. Font^{1,3}

¹*Departamento de Astronomía y Astrofísica, Universitat de València, Dr. Moliner 50, E-46100 Burjassot (València), Spain*

²*Departament de Física Aplicada, Universitat d'Alacant, Ap. Correus 99, E-03080 Alacant, Spain*

³*Observatori Astronòmic, Universitat de València, Catedrático José Beltrán 2, E-46980 Paterna (València), Spain*

Accepted 2015 December 10. Received 2015 December 10; in original form 2015 November 10

ABSTRACT

The observation of several neutron stars in the centre of supernova remnants and with significantly lower values of the dipolar magnetic field than the average radio-pulsar population has motivated a lively debate about their formation and origin, with controversial interpretations. A possible explanation requires the slow rotation of the protoneutron star at birth, which is unable to amplify its magnetic field to typical pulsar levels. An alternative possibility, the hidden magnetic field scenario, considers the accretion of the fallback of the supernova debris on to the neutron star as responsible for the submergence (or screening) of the field and its apparently low value. In this paper, we study under which conditions the magnetic field of a neutron star can be buried into the crust due to an accreting, conducting fluid. For this purpose, we consider a spherically symmetric calculation in general relativity to estimate the balance between the incoming accretion flow and the magnetosphere. Our study analyses several models with different specific entropy, composition, and neutron star masses. The main conclusion of our work is that typical magnetic fields of a few times 10^{12} G can be buried by accreting only 10^{-3} – $10^{-2} M_{\odot}$, a relatively modest amount of mass. In view of this result, the central compact object scenario should not be considered unusual, and we predict that anomalously weak magnetic fields should be common in very young ($< \text{few kyr}$) neutron stars.

Key words: stars: magnetic field – stars: neutron – pulsars: general.

1 INTRODUCTION

Central compact objects (CCOs) are isolated, young neutron stars (NSs) which show no radio emission and are located near the centre of young supernova remnants (SNRs). Three such NSs, PSR E1207.4–5209, PSR J0821.0–4300, and PSR J1852.3–0040, show an inferred magnetic field significantly lower than the standard values for radio pulsars (i.e. 10^{12} G). The main properties of these sources are summarized in Table 1. In all cases, the difference between the characteristic age of the NS $\tau_c = P/\dot{P}$ and the age of the SNR indicates that these NSs were born spinning at nearly their present periods ($P \sim 0.1$ – 0.4 s). This discovery has challenged theoretical models of magnetic field generation, which need to be modified to account for their peculiar properties.

The first possible explanation for the unusual magnetic field found in these objects simply assumes that these NSs are born with a magnetic field much lower than that of their classmates. This value can be amplified by turbulent dynamo action during the protoneutron star (PNS) phase (Thompson & Duncan 1993; Bonanno, Urpin & Belvedere 2005). In this model, the final low values of the magnetic field would reflect the fact that the slow rotation of the NS

at birth does not suffice to effectively amplify the magnetic field through dynamo effects. However, recent studies have shown that, even in the absence of rapid rotation, magnetic fields in PNS can be amplified by other mechanisms such as convection and the standing accretion shock instability (Endeve et al. 2012; Obergaulinger, Janka & Aloy-Torás 2014).

An alternative explanation is the hidden magnetic field scenario (Muslimov & Page 1995; Young & Channugan 1995; Geppert, Page & Zannias 1999; Shabaltas & Lai 2012). Following the supernova explosion and the NS birth, the supernova shock travels outwards through the external layers of the star. When this shock crosses a discontinuity in density, it is partially reflected and moves backwards (reverse shock). The total mass accreted by the reverse shock in this process is in the range from $\sim 10^{-4} M_{\odot}$ to a few solar masses on a typical time-scale of hours to days (Ugliano et al. 2012). Such a high accretion rate can compress the magnetic field of the NS which can eventually be buried into the NS crust. As a result, the value of the external magnetic field would be significantly lower than the internal ‘hidden’ magnetic field. Bernal, Lee & Page (2010) performed 1D and 2D numerical simulations of a single column of material falling on to a magnetized NS and showed how the magnetic field can be buried into the NS crust.

Once the accretion process stops, the magnetic field might eventually re-emerge. The initial studies investigated the process of

*E-mail: Alejandro.Torres@uv.es

Table 1. CCOs in SNRs. From left to right, the columns indicate the name of the CCO, the age, the distance d , the period P , the inferred surface magnetic field, B_s , the bolometric luminosity in X-rays, $L_{x, \text{bol}}$, the name of the remnant, the characteristic age, and bibliographical references.

CCO	Age (kyr)	d (kpc)	P (s)	B_s 10^{11}G	$L_{x, \text{bol}}$ (erg s^{-1})	SNR	τ_c (Myr)	References
J0822.0–4300	3.7	2.2	0.112	0.65	6.5×10^{33}	Puppis A	190	1, 2
1E 1207.4–5209	7	2.2	0.424	2	2.5×10^{33}	PKS 1209-51/52	310	2, 3, 4, 5, 6, 7
J185238.6+004020	7	7	0.105	0.61	5.3×10^{33}	Kes 79	190	8, 9, 10, 11

References: (1) Hui & Becker (2006), (2) Gotthelf, Halpern & Alford (2013), (3) Zavlin et al. (2000), (4) Mereghetti et al. (2002), (5) Bignami et al. (2003), (6) De Luca et al. (2004), (7) Gotthelf & Halpern (2007), (8) Seward et al. (2003), (9) Gotthelf, Halpern & Seward (2005), (10) Halpern et al. (2007), (11) Halpern & Gotthelf (2010).

re-emergence using simplified 1D models and dipolar fields (Muslimov & Page 1995; Young & Chanmugan 1995; Geppert et al. 1999) and established that the time-scale for the magnetic field re-emergence is $\sim 1\text{--}10^7$ kyr, critically depending on the depth at which the magnetic field is buried. More recent investigations have confirmed this result. Ho (2011) observed similar time-scales for the re-emergence using a 1D cooling code. Viganò & Pons (2012) carried out simulations of the evolution of the interior magnetic field during the accretion phase and the magnetic field submergence phase.

In the present work, we study the feasibility of the hidden magnetic field scenario using a novel numerical approach based on the solutions of 1D Riemann problems (discontinuous initial value problems) to model the compression of the magnetic field of the NS. The two initial states for the Riemann problem are defined by the magnetosphere and by the accreting fluid, at either sides of a moving, discontinuous interface. Following the notation defined in Michel (1977), the NS magnetosphere refers to the area surrounding the star where the magnetic pressure dominates over the thermal pressure of the accreting fluid. The magnetopause is the interface between the magnetically dominated area and the thermally dominated area. The equilibrium point is defined as the radius at which the velocity of the contact discontinuity is zero.

The paper is organized as follows. In Sections 2–5, we present the model we use to perform our study. We describe in these sections the equation of state (EoS) of the accreting fluid, the spherically symmetric Michel solution characterizing the accreting fluid, and all the expressions needed to compute the potential solution for the magnetic field in the magnetosphere. Section 6 contains the main results of this work. After establishing a reference model, we vary the remaining parameters, namely entropy, composition, and the initial distribution of the magnetic field, and study their influence on the fate of the magnetic field. Finally, in Section 7 we summarize the main results of our study and present our conclusions and plans for future work. If not explicitly stated otherwise, we use units of $G = c = 1$. Greek indices (μ, ν, \dots) run from 0 to 3 and Latin indices (i, j, \dots) from 1 to 3.

2 THE REVERSE SHOCK AND THE FALLBACK SCENARIO

At the end of their lives, massive stars ($M_{\text{star}} \gtrsim 8 M_{\odot}$) possess an onion-shell structure as a result of successive stages of nuclear burning. An inner core, typically formed by iron, with a mass of $\sim 1.4 M_{\odot}$ and ~ 1000 km radius develops at the centre, balancing gravity through the pressure generated by a relativistic, degenerate, $\gamma = 4/3$, fermion gas. The iron core is unstable due to photodisintegration of nuclei and electron captures, which result in a deleptonization of the core and a significant pressure reduction ($\gamma < 4/3$). As a result, the core shrinks and collapses gravitationally

to nuclear matter densities on dynamical time-scales (~ 100 ms). As the centre of the star reaches nuclear saturation density ($\sim 2 \times 10^{14} \text{ g cm}^{-3}$), the EoS stiffens and an outward-moving (prompt) shock is produced. As it propagates out, the shock suffers severe energy losses dissociating Fe nuclei into free nucleons ($\sim 1.7 \times 10^{51} \text{ erg}/0.1 M_{\odot}$), consuming its entire kinetic energy inside the iron core (it stalls at $\sim 100\text{--}200$ km), becoming a standing accretion shock in a few ms. There is still debate about the exact mechanism and conditions for a successful explosion, but it is commonly accepted that the standing shock has to be revived on a time-scale of $\lesssim 1$ s by the energy deposition of neutrinos streaming out of the innermost regions, and some form of convective transport for the shock to carry sufficient energy to disrupt the whole star (see Janka et al. 2007, for a review on the topic).

Even if the shock is sufficiently strong to power the supernova, part of the material between the nascent NS and the propagating shock may fall back into the NS (Colgate 1971; Chevalier 1989). Determining the amount of fallback material depends not only on the energy of the shock but also on the radial structure of the progenitor star (Fryer 2006). Most of the fallback accretion is the result of the formation of an inward-moving reverse shock produced as the main supernova-driving shock crosses the discontinuity between the helium shell and the hydrogen envelope (Chevalier 1989). For typical supernova progenitors ($10\text{--}30 M_{\odot}$), the base of the hydrogen envelope is at $r_{\text{H}} \sim 10^{11}\text{--}3 \times 10^{12}$ cm (Woosley, Heger & Weaver 2002), which is reached by the main shock on a time-scale of a few hours. The reverse shock travels inwards carrying mass that accretes on to the NS. It reaches the vicinity of the NS on a time-scale of hours, about the same time at which the main supernova shock reaches the surface of the star (Chevalier 1989). By the time the reverse shock reaches the NS, the initially hot PNS has cooled down significantly. In its first minute of life, the PNS contracts, cools down to $T < 10^{10}$ K, and becomes transparent to neutrinos (Burrows & Lattimer 1986; Pons et al. 1999). In the next few hours, the inner crust ($\rho \in [2 \times 10^{11}, 2 \times 10^{14}] \text{ g cm}^{-3}$) solidifies but the low-density envelope ($\rho < 2 \times 10^{11} \text{ g cm}^{-3}$), which will form the outer crust on a time-scale of 1–100 yr, remains fluid (Page et al. 2004; Aguilera, Pons & Miralles 2008).

Understanding the processes generating the magnetic field observed in NSs, in the range from $\sim 10^{10}$ G to $\sim 10^{15}$ G, is still an open issue. Most likely, convection, rotation, and turbulence during the PNS phase play a crucial role in field amplification (Thompson & Duncan 1993). However, at the time in the evolution that we are considering (hours after birth), none of these processes can be active anymore and the electric current distribution generating the magnetic field will be frozen in the interior of the NS. These currents evolve now on the characteristic Hall and Ohmic time-scales of $10^4\text{--}10^6$ yr (Pons & Geppert 2007; Pons, Miralles & Geppert 2009; Viganò et al. 2013), much longer than the time-scale t_{acc} during

which fallback is significant, which can be estimated as the free-fall time from the base of the hydrogen envelope

$$t_{\text{acc}} \sim \frac{1}{2} \left(\frac{r_{\text{H}}^3}{GM} \right)^{1/2}. \quad (1)$$

This ranges from 30 min to several days for the typical values of r_{H} and $M = 1.4 M_{\odot}$.

The total mass accreted during this phase is more uncertain. Detailed 1D numerical simulations of the shock propagation and fallback estimate that typical values range from $10^{-4} M_{\odot}$ to a few solar masses (Woosley & Weaver 1995; Zhang, Woosley & Heger 2008; Ugliano et al. 2012). If more than a solar mass is accreted, the final outcome would be the delayed formation of a black hole, hours to days after core bounce. Chevalier (1989) and Zhang et al. (2008) showed that the accretion rate is expected to be maximum when the reverse shock reaches the NS and decreases as $t^{-5/3}$ at later times. Therefore, the total amount of accreted mass is dominated by the fallback during the first few hours. Given the theoretical uncertainties, we assume for the rest of this work that a total mass of $\delta M \in [10^{-5} M_{\odot}, \delta M_{\text{max}}]$ is accreted during a typical time-scale of $t_{\text{acc}} \in [10^3, 10^4]$ s, being $\delta M_{\text{max}} \sim 1 M_{\odot}$ the amount of mass necessary to add to the NS to form a black hole. Therefore, the typical accretion rate during fallback is $\dot{M} \in [10^{-9}, 10^{-3}] M_{\odot} \text{ s}^{-1}$, which, for practical purposes, we assume to stay constant during the accretion phase. This accretion rate, even at its lowest value, exceeds by far the Eddington luminosity

$$\frac{\dot{M} c^2}{L_{\text{Edd}}} = 5 \times 10^6 \left(\frac{\dot{M}}{10^{-9} M_{\odot} \text{ s}^{-1}} \right), \quad (2)$$

with $L_{\text{Edd}} = 3.5 \times 10^{38} \text{ erg s}^{-1}$ the Eddington luminosity for electron scattering.

In the hypercritical accretion regime, the optical depth is so large that photons are advected inwards with the flow faster than they can diffuse outwards (Blondin 1986; Chevalier 1989; Houck & Chevalier 1991). As a result, the accreting material cannot cool down resulting in an adiabatic compression of the fluid. The dominant process cooling down the accreting fluid and releasing the energy stored in the infalling fluid is neutrino emission (Houck & Chevalier 1991). At temperatures above the pair creation threshold, $T_{\text{pair}} \approx 10^{10} \text{ K}$, pair annihilation can produce neutrino–antineutrino pairs, for which the infalling material is essentially transparent and are able to cool down very efficiently the material as it is decelerated at the surface of the NS or at the magnetopause. Therefore, the specific entropy, s , of the fallback material remains constant all through the accretion phase until it decelerates in the vicinity of the NS.

The value for s is set at the time of the reverse shock formation. Detailed 2D numerical simulations of the propagation of the shock through the star (Kifonidis et al. 2003, 2006; Scheck et al. 2006) show that typical values of $s \sim 20 k_{\text{B}}/\text{nuc}$ are found at the reverse shock. At this stage of the explosion, the flow is highly anisotropic due to the Rayleigh–Taylor instability present in the expanding material and the Richtmyer–Meshkov instability at the He/H interface. Those instabilities generate substantial mixing between hydrogen and helium and even clumps of high-entropy heavier elements (from C to Ni) rising from the innermost parts of the star. Therefore, the fallback material has entropy in the range $s \sim 1\text{--}100 k_{\text{B}}/\text{nuc}$ and its composition, although it is mostly helium, can contain almost any element present in the explosion. 3D simulations show qualitatively similar results regarding the entropy values and mixing (Hammer, Janka & Müller 2010; Joggerst, Almgren & Woosley 2010; Wongwathanarat, Müller & Janka 2015).

Outside the NS, the expanding supernova explosion leaves behind a low-density rarefaction wave which is rapidly filled by the NS magnetic field, forming the magnetosphere. For the small magnetospheric densities, the inertia of the fluid can be neglected, and the magnetosphere can be considered force-free. The fallback reverse shock propagates inwards compressing this magnetosphere. The boundary between the unmagnetized material falling back and the force-free magnetosphere, i.e. the magnetopause, can be easily compressed at long distances ($r \gtrsim 10^8 \text{ cm}$) due to the large difference of the pressure of the infalling material with respect to the magnetic pressure. The dynamical effect of the magnetosphere only plays a role at $r \lesssim 10^8 \text{ cm}$, i.e. inside the light cylinder for most cases. The precise radius where the magnetic field becomes dynamically relevant is estimated later in Section 5.2. Only in the case of magnetar-like magnetic fields and fast initial spin ($P \lesssim 10 \text{ ms}$), this consideration is not valid, although this is not the case for CCOs.

To conclude this scenario overview, we note that the magnetospheric torques will spin down the NS on a characteristic time-scale (Shapiro & Teukolsky 2004) given by

$$\tau_{\text{c}} = \frac{P}{2\dot{P}} \sim 180 \left(\frac{B_{\text{p}}}{10^{15} \text{ G}} \right)^{-2} \left(\frac{P}{1 \text{ s}} \right)^2 \text{ yr}, \quad (3)$$

for a typical NS with radius 10 km and mass $1.4 M_{\odot}$. B_{p} is the value of the magnetic field at the pole of the NS. The value of the moment of inertia is $1.4 \times 10^{45} \text{ g cm}^2$. At birth, the spin period of an NS is limited by the mass-shedding limit to be $P > 1 \text{ ms}$ (Goussard, Haensel & Zdunik 1998). If all NSs were born with millisecond periods, purely magneto-dipolar spin-down would limit the observed period of young NSs (10^4 yr) to

$$P_{\text{obs}, 10^4 \text{ yr}} \lesssim 5.5 \left(\frac{B}{10^{15} \text{ G}} \right)^2 \text{ s}. \quad (4)$$

For magnetic fields $B \lesssim 1.4 \times 10^{13} \text{ G}$, this criterion fails for the vast majority of pulsars and all CCOs ($P \gtrsim 0.1 \text{ s}$) and therefore the measured spin period must be now very close to that hours after the onset of the supernova explosion. Detailed population synthesis studies of the radio-pulsar population clearly favour a broad initial period distribution in the range 0.1–0.5 s (Faucher-Giguère & Kaspi 2006; Gullón et al. 2014), rather than fast millisecond pulsars. Therefore, from observational constraints, it is reasonable to assume that progenitors of pulsars (including CCOs) have spin periods of $P \sim 0.1\text{--}0.5 \text{ s}$ at the moment of fallback. For such low rotation rates, the NS can be safely considered as a spherically symmetric body and its structure can thus be computed by solving the Tolman–Oppenheimer–Volkoff (TOV) equation.

3 STATIONARY SPHERICAL ACCRETION

We model the fallback of the reverse shock as the spherically symmetric accretion of an unmagnetized relativistic fluid. The stationary solutions for this system were first obtained by Michel (1972) for the case of a polytropic EoS. Here, we extend this work to account for a general (microphysically motivated) EoS. The equations that describe the motion of matter captured by a compact object, i.e. an NS or black hole, can be derived directly from the equations of relativistic hydrodynamics, namely the conservation of rest mass,

$$\nabla_{\mu} J^{\mu} = 0, \quad (5)$$

and the conservation of energy-momentum,

$$\nabla_{\mu} T^{\mu\nu} = 0, \quad (6)$$

where we use the notation ∇_μ for the covariant derivative and the density current J^μ and the (perfect fluid) energy-momentum tensor $T^{\mu\nu}$ are given by

$$J^\mu = \rho u^\mu, \quad (7)$$

$$T_{\mu\nu} = \rho h u_\mu u_\nu + p g_{\mu\nu}. \quad (8)$$

In the above equations, ρ is the rest-mass density, p is the pressure, and h is the specific enthalpy, defined by $h = 1 + \varepsilon + p/\rho$, where ε is the specific internal energy, u^μ is the four-velocity of the fluid, and $g_{\mu\nu}$ defines the metric of the general space-time where the fluid evolves. Assuming spherical symmetry and a steady state, we have

$$\frac{d}{dr}(J^1 \sqrt{-g}) = 0, \quad (9)$$

$$\frac{d}{dr}(T_0^1 \sqrt{-g}) = 0, \quad (10)$$

where $g \equiv \det(g_{\mu\nu})$. The exterior metric of a non-rotating compact object is given by the Schwarzschild metric

$$ds^2 = -\left(1 - \frac{2M}{r}\right) dt^2 + \left(1 - \frac{2M}{r}\right)^{-1} dr^2 + r^2(d\theta^2 + \sin^2\theta d\varphi^2). \quad (11)$$

In Schwarzschild coordinates, equations (9) and (10) can be easily integrated to obtain (cf. Michel 1972)

$$\rho u r^2 = C_1, \quad (12)$$

$$h^2 \left(1 - \frac{2M}{r} + u^2\right) = C_2, \quad (13)$$

where C_1 and C_2 are integration constants and $u \equiv u^r$. To obtain an adiabatic solution for the accreting fluid, we differentiate equations (12) and (13) at constant entropy and eliminate $d\rho$,

$$\begin{aligned} \frac{du}{u} \left[V^2 - u^2 \left(1 - \frac{2M}{r} + u^2\right)^{-1} \right] \\ + \frac{dr}{r} \left[2V^2 - \frac{M}{r} \left(1 - \frac{2M}{r} + u^2\right)^{-1} \right] = 0, \end{aligned} \quad (14)$$

where

$$V^2 \equiv \frac{\rho}{h} \frac{\partial h}{\partial \rho} \Big|_s. \quad (15)$$

The solutions of this equation are those passing through a critical point where both terms in brackets in equation (14) are zero, i.e. those fulfilling

$$\begin{aligned} 2u_c^2 &= \frac{M}{r_c}, \\ V_c^2 &= u_c^2 (1 - 3u_c^2)^{-1}, \end{aligned} \quad (16)$$

where sub-index ‘c’ indicates quantities evaluated at the critical point. The critical point can be identified as the sonic point, i.e. the point where the velocity of the fluid equals its own sound speed. After some algebra, it can be shown that the constant C_1 in equation (12) is related to the accretion rate \dot{M} by

$$\dot{M} = -4\pi C_1. \quad (17)$$

Thereby we can obtain the accretion solution by simply selecting the mass accretion rate and the specific entropy of the fluid, which

fixes the two constants C_1 and C_2 . We note that, for each pair of values, the system (16) has two solutions, although only one represents a physical accretion solution ($|u| \rightarrow 0$ at $r \rightarrow \infty$). In this case, the fluid is supersonic for radii below the critical radius and subsonic above. Fig. 1 displays one illustrative accretion solution for a mass accretion rate $\dot{M} = 10^{-5} M_\odot \text{ s}^{-1}$ and entropy per baryon $s = 80 k_B/\text{nuc}$.

For the accreting material, we use the tabulated Helmholtz EoS (Timmes & Swesty 2000), which is an accurate interpolation of the Helmholtz free energy of the Timmes EoS (Timmes & Arnett 1999). Timmes EoS, and Helmholtz EoS by extension, includes the contributions from ionized nuclei, electrons, positrons, and radiation. By default, Timmes EoS uses the rest-mass density ρ [g cm^{-3}], temperature T [K], and composition as input. For convenience, we have developed a search algorithm that allows us to call the EoS with different thermodynamical variables as input (e.g. ρ , s , and composition as inputs for the adiabatic flow of accreting material). Helmholtz EoS also requires the mean mass number \bar{A} and the mean atomic number \bar{Z} .

At low densities, $\rho < 6 \times 10^7 \text{ g cm}^{-3}$, and temperatures, $T \lesssim 2 \times 10^9 \text{ K}$, nuclear reactions proceed much slower than the accretion time-scale and the composition remains frozen during the accretion. We fix the composition to that at the reverse shock formation point. Given the uncertainties, we consider two possibilities in this regime, either pure helium or pure carbon. At temperatures $T \gtrsim 2 \times 10^9 \text{ K}$, nuclear burning becomes fast enough to change the composition. For $T \gtrsim 4 \times 10^9 \text{ K}$, the fluid reaches nuclear statistical equilibrium (NSE) on a significantly shorter time-scale than the accretion time-scale (see e.g. Woosley et al. 2002). To deal with the high-temperature regime, $T \geq 2 \times 10^9 \text{ K}$, we have tried three different approaches: (1) unchanged composition of the accreting material, (2) compute the NSE composition at a given temperature and density using a thermonuclear reaction network with 47 isotopes (Timmes 1999; Seitenzahl 2008) and (3) simplified burning with four transitions: ${}^4\text{He}$ for $T \leq 2 \times 10^9 \text{ K}$, ${}^{56}\text{Ni}$ for $2 \times 10^9 > T \geq 5 \times 10^9 \text{ K}$, ${}^4\text{He}$ for $5 \times 10^9 > T \geq 2 \times 10^{10} \text{ K}$, and protons and neutrons for $T > 2 \times 10^{10} \text{ K}$. We use the publicly available routines of the Helmholtz EoS and the NSE equilibrium kindly provided by the authors.¹

4 NON-MAGNETIZED ACCRETION AND PILE-UP

Before considering the case of magnetized accretion on to an NS, we study the case of non-magnetized accretion. For the span of accretion rates considered in this work, the sonic point of the accreted fluid is located at $r > 23\,500 \text{ km}$ at entropy $s = 10 k_B/\text{nuc}$, and hence the fallback material falls supersonically on to the NS. Inevitably, an accretion shock forms at the surface of the star, which propagates outwards. The accreted fluid crossing the shock will heat up, increasing its specific entropy and will fall subsonically. The high entropy of this material ($s_{\text{shock}} \in [70\text{--}300] k_B/\text{nuc}$) and the compression that experiments as it flows inwards raise the temperature beyond the pair creation threshold, $T_{\text{pair}} \approx 10^{10} \text{ K}$, and the fluid will cool efficiently via neutrino–antineutrino annihilation. Therefore, the kinetic energy of the supersonically accreting fluid is mostly transformed into thermal energy as it crosses the accretion shock and then is dissipated to neutrinos close to the NS surface. Chevalier (1989) showed that the accretion shock will eventually

¹ http://cococubed.asu.edu/code_pages/codes.shtml

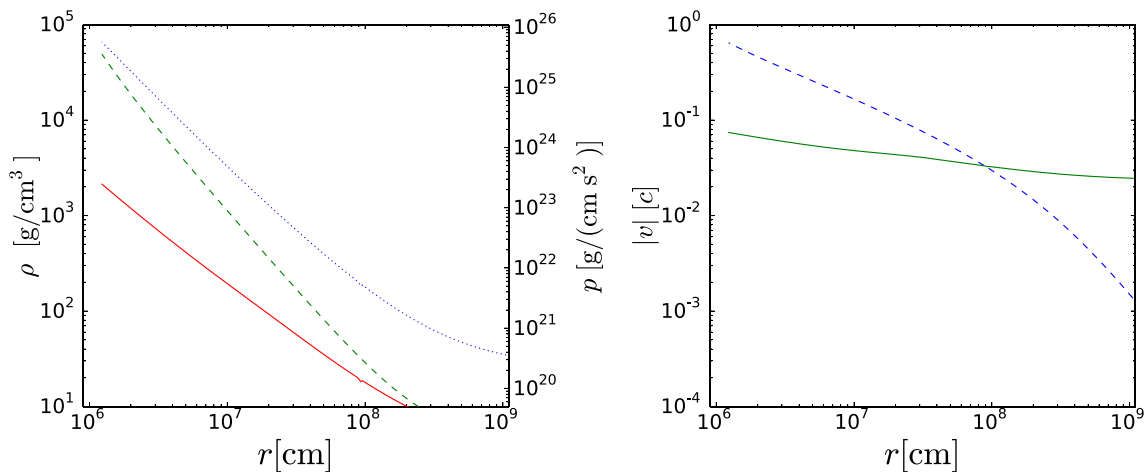


Figure 1. Illustrative accretion solution for an accretion rate $\dot{M} = 10^{-5} M_{\odot} \text{ s}^{-1}$ and entropy per baryon $s = 80k_B/\text{nuc}$. The left-hand panel shows the density (green dashed line, left axis), pressure (red solid line, right axis), and ram pressure (blue dotted line, right axis). The right-hand panel shows the absolute value of the fluid velocity (blue dashed line) and the sound speed (green solid line). The two lines cross at the critical point.

stall at a certain radius as an energy balance is found. The radius of the stalled shock depends only on the accretion rate \dot{M} and is located at about $R_{\text{shock}} \sim 10^7\text{--}10^8$ km. In some estimates below in this work, we use the values provided in table 1 in Houck & Chevalier (1991), based on a more realistic treatment of the accretion and neutrino cooling.

The final fate of the neutrino-cooled material falling steadily on to the NS surface is to pile up on top of the original NS material forming a layer of new material. In order to study the effect of the pile-up, we consider an NS of mass M and radius R . If we add a mass δM to the equilibrium model, the new NS will have a new radius R_{new} smaller than the original one. The original surface of the star will now be buried at a depth δR , i.e. the new surface will be located at a distance δR over the old surface. Although trivial, the last statement is important because most of the discussion below in this work is carried out in terms of δR and in terms of distances with respect to the original NS surface. Therefore, it makes sense to try to compute what is the dependence of the burial depth, δR , with the total accreted mass, δM . In order to compute this dependence, we use the TOV equations to solve a sequence of NS equilibrium models starting with M and progressively increasing to $M + \delta M$ for different values of δM . For each model in the sequence, we compute δR as the distance between the radius enclosing a mass M and the surface of the star, i.e. the radius enclosing $M + \delta M$. Given the small values of δM , we integrate the TOV equations using a simple forward Euler method, with a step limited to relative variations of density of 10^{-5} and a maximum step of 10 cm. We have computed the relation between δR and δM for five different NS masses, $M = 1.2, 1.4, 1.6, 1.8,$ and $2.0 M_{\odot}$. We have used several realistic EoS in tabulated form, namely four different combinations using either EoS APR (Akmal, Pandharipande & Ravenhall 1998) or EoS L (Pandharipande & Smith 1975) for the core and EoS NV (Negele & Vautherin 1973) or EoS DH (Douchin & Haensel 2001) for the crust. For each case, we compute the sequence up to the maximum mass; beyond that mass, the equilibrium model is unstable and it will collapse to a black hole in dynamical time-scales. All EoS allow for equilibrium solutions with maximum mass consistent with recent observations of an NS with mass close to $2 M_{\odot}$ (Demorest et al. 2010; Antoniadis et al. 2013). The blue solid line in Fig. 2 shows the dependence of δR with δM for a $1.4 M_{\odot}$ NS with the APRDH EoS. All other EoS and NS masses show similar behaviour. For all

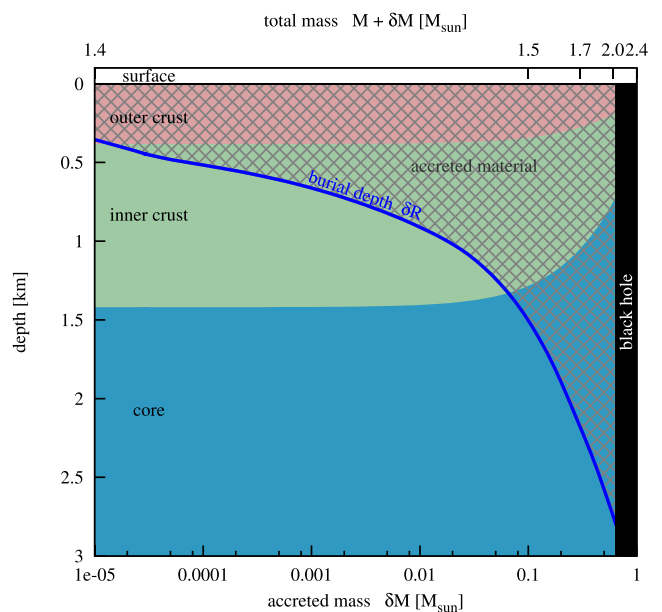


Figure 2. Dependence of the burial depth (blue solid lines), δR , with the accreted mass, δM (bottom axis), for an $M = 1.4 M_{\odot}$ NS using APRDH EoS. Note that positive values of the depth increase downwards. Regions occupied by the outer crust, inner crust, and core appear with different colours and labelled. The region occupied by the accreted material is plotted with a grey crosshatch pattern. The top axis shows the total mass of the NS after accretion, $M + \delta M$. Above $M = 2.25 M_{\odot}$, the configuration is unstable and the object will collapse to a black hole.

EoS, any amount of accreted mass larger than $\sim 10^{-4} M_{\odot}$ will sink the original NS surface to the inner crust, and for $\delta M \sim 0.1 M_{\odot}$ the entire crust is formed by newly accreted material. The bottom line is that, if the accreted material is able to compress the magnetosphere and deposit itself on top of the NS, the magnetic field trapped with the fluid may be buried into the NS crust, and depending on the conditions (accreted mass and magnetic field strength), the burial depth could be as deep as the inner crust. We study next the impact of magnetic fields in the vicinity of the NS, namely the magnetosphere, in the burial process.

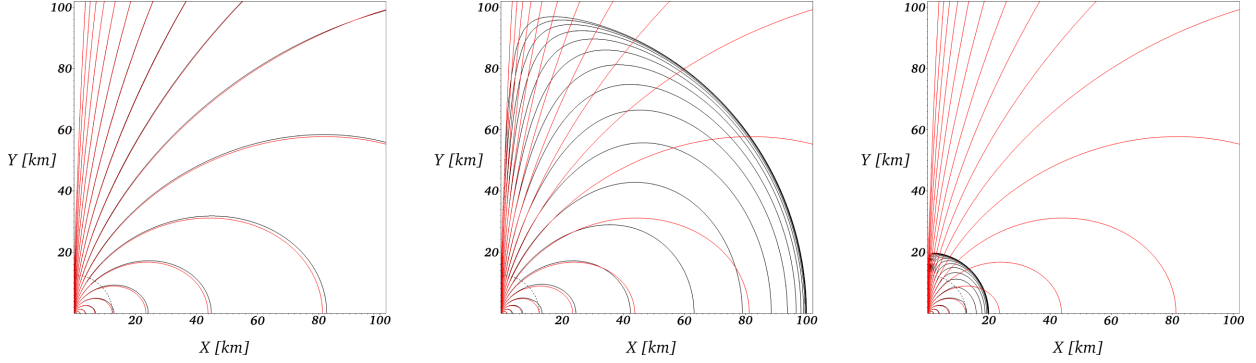


Figure 3. Magnetic field lines (black lines) for three different positions of the magnetopause for the same initial distribution of the magnetic field (red lines) with $B_p = 10^{13}$ G. The dashed line represents the NS surface.

5 MAGNETOSPHERE

5.1 Potential magnetospheric solution

For simplicity in the following discussion, we use a *reference model* with the APRDH EoS and $M = 1.4 M_\odot$. This model results in an NS with coordinate radius $R = 12.25$ km. The effect of the EoS and the NS mass is discussed later in the text. Given that both the magnetosphere and the accreted material involve low energy densities compared with those inside the NS, the space–time outside the NS can be regarded as non-self-gravitating and approximated by the Schwarzschild exterior solution.

The magnetosphere extends between the NS surface and the magnetopause, which will be assumed to be a spherically symmetric surface at the location of the infalling reverse shock. We model this region using the force-free magnetic field approximation, $\mathbf{J} \times \mathbf{B} = 0$, \mathbf{J} being the electric current and \mathbf{B} the magnetic field. We neglect the currents resulting from the rotation of the star. Consequently, the magnetic field has a potential solution, solution of the relativistic Grad–Shafranov equation. In spherical coordinates, the magnetic field vector components are related to the vector potential A as

$$\hat{B}_r = \frac{1}{r^2 \sin \theta} \partial_\theta A_\phi, \quad (18)$$

$$\hat{B}_\theta = \frac{-1}{r^2 \sin \theta} \partial_r A_\phi, \quad (19)$$

$$\hat{B}_\phi = 0, \quad (20)$$

where $\hat{B}_i = \sqrt{\gamma} B_i$ and γ is the determinant of the spatial metric. If we assume axisymmetry, the unique non-zero component of the electric current is the ϕ component,

$$J_\phi = \sin \theta [\partial_r (r \hat{B}_\theta) - \partial_\theta \hat{B}_r]. \quad (21)$$

Imposing the force-free condition, we obtain

$$-J_\phi \hat{B}_\theta = 0, \quad (22)$$

$$J_\phi \hat{B}_r = 0. \quad (23)$$

Since $\hat{B}_r, \hat{B}_\theta \neq 0$, the only possible solution is $J_\phi = 0$. As we want an expression that only depends on the vector potential, we replace equations (18) and (19) in equation (21) resulting in

$$\begin{aligned} J_\phi &= \sin \theta \left[\frac{-1}{\sin \theta} \partial_r (\partial_r A_\phi) - \frac{1}{r^2} \partial_\theta \left(\frac{\partial_\theta A_\phi}{\sin \theta} \right) \right] \\ &= -\partial_{rr} A_\phi - \frac{1}{r^2} \partial_{\theta\theta} A_\phi + \frac{\cot \theta}{r^2} \partial_\theta A_\phi = 0. \end{aligned} \quad (24)$$

We discretize this expression using second-order finite differences and solve the resulting linear system of equations using a cyclic reduction algorithm (Swarztrauber 1974). We impose Dirichlet boundary conditions on A_ϕ at the surface of the NS to match with the interior value of the radial component of the magnetic field. Our aim is to describe a magnetosphere, which is confined within a certain radius, R_{mp} , defining the magnetopause. Magnetic field lines at the magnetopause are parallel to this interface and they enter the NS along the axis. Therefore, they correspond to lines with $A_\phi = 0$, which we use as Dirichlet boundary condition at R_{mp} to solve the Grad–Shafranov equation. We can obtain the field distribution after the compression by simply changing the radius where the boundary conditions are imposed. The evolution of the magnetic field geometry before and after compression is shown in Fig. 3 for three illustrative cases.

For the interior magnetic field, which determines the boundary conditions at the surface of the star, we use two different magnetic field distributions, a dipolar magnetic field (*dipole* hereafter) and a poloidal field generated by a circular loop of radius $r = 4 \times 10^5$ cm (Jackson 1962, *loop current* hereafter). Following Gabler et al. (2012), it is useful to introduce the *equivalent magnetic field*, B^* , which we define as the magnetic field strength at the surface of a Newtonian, uniformly magnetized sphere with radius 10 km having the same dipole magnetic moment as the configuration we want to describe. It spans the range $B^* \in [10^{10} - 10^{16}]$ G.

5.2 Magnetosphere compression

In the case of a fluid accreting on to a force-free magnetosphere, the magnetopause will remain spherical and will move inwards as long as the total pressure of the unmagnetized fluid, $p_{\text{tot}} = p + p_{\text{ram}}$, exceeds that of the magnetic pressure, p_{mag} , of the magnetosphere. If we approximate the magnetopause as a spherical boundary between the spherically symmetric accreting solution described in Section 3 and the potential solution computed in Section 5.1, its properties can be described as the solution of a Riemann problem at the magnetopause. Since the magnetic field of the initial state is tangential to the magnetopause, we can use the exact solution of the Riemann problem developed by Romero et al. (2005). A succinct summary of the details of the implementation of the Riemann solver can be found in Appendix A.

For illustrative purposes, the left-hand panel of Fig. 4 shows the solution of the Riemann problem for a supersonic fluid accreting from the right into a magnetically dominated region (magnetosphere) on the left. The figure displays both the density (left axis, solid lines) and the fluid velocity (right axis, dashed lines). The

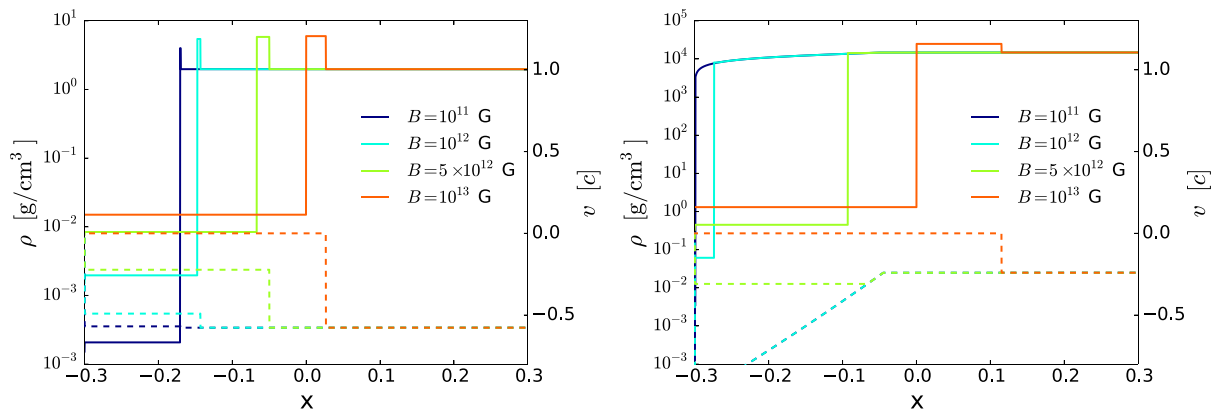


Figure 4. Density (solid lines, left axis) and velocity (dashed lines, right axis) profiles of the solution of the Riemann problem for several values of the magnetic field. Initially, the discontinuity is set at $x = 0$, an accreting fluid at $x > 0$, and a magnetized fluid at $x < 0$, with constant magnetic field B . The left-hand panel shows the case of supersonic accretion of a fluid with specific entropy $s = 10k_B/\text{nuc}$ and $\dot{M} = 10^{-7} M_\odot \text{ s}^{-1}$ at $t = 0.3$ s. The right-hand panel shows the case of subsonic accretion of a fluid with $s = 2000k_B/\text{nuc}$ and $\dot{M} = 10^{-5} M_\odot \text{ s}^{-1}$ at $t = 0.3$ s.

initial discontinuity is located at $x = 0$. The right constant state of the Riemann problem corresponds to the accreting fluid with an entropy of $s = 10k_B/\text{nuc}$ and accretion rate of $\dot{M} = 10^{-7} M_\odot \text{ s}^{-1}$. The left constant state corresponds to a state with magnetic pressure $B^2/2$. The figure plots the corresponding solutions for different values of B around the equilibrium (indicated in the legend).

Looking at the left-hand panel of Fig. 4 from left to right, the first jump in density corresponds to the contact discontinuity, point at which, as expected, the velocity remains continuous. The next discontinuity is a shock wave, where both the density and velocity are discontinuous, and both decrease. For low magnetic fields, $B \leq 10^{10}$ G, the low magnetic pressure on the left state cannot counteract the total pressure of the accreting fluid and the contact discontinuity advances to the right at a velocity equal to that of the accreting fluid; a shock front is practically non-existent. As the magnetic field is increased, the velocity of the contact discontinuity decreases and it becomes zero at about $B = 10^{13}$ G. We identify this point as the *equilibrium point*, since no net flux of matter crosses $x = 0$. Around this equilibrium point, an accretion shock appears, which heats and decelerates matter coming from the right. The equilibrium point corresponds to a solution in which the matter crossing the shock has zero velocity, i.e. it piles up on top of the left state as the shock progresses to the right.

The actual accretion of matter on to a magnetically dominated magnetosphere is expected to behave in a similar way as the described Riemann problem. At large distances (low B), the magnetopause (contact discontinuity) is compressed at the speed of the fluid. As the magnetosphere is compressed, the magnetic field strength rises and at some point an equilibrium point is found, beyond which the magnetosphere impedes the accretion of the fluid.

In the right-hand panel of Fig. 4, we show for the sake of completeness the solution for a subsonic accreting fluid. In accreting NS, this regime is probably unrealistic, since very large specific entropy is necessary ($s = 2000k_B/\text{nuc}$ in the example plotted). In this case, the solution is qualitatively different; instead of a shock, a rarefaction wave is formed for B below the equilibrium point. For larger values of B , an accretion shock is formed.

5.3 Setup

Our goal is to study the conditions under which the magnetic field of a newborn NS can be buried by fallback material during a supernova.

We have spanned a large range of values for both, the magnetic field strength and the accretion rate, proceeding as follows. We obtain the distance from the NS surface where the magnetosphere and the accreting fluid are in balance, i.e. the radial point where the velocity of the contact discontinuity is zero. We reduce our 2D configuration to a 1D Riemann problem by restricting the evaluation of the equilibrium point to the equatorial plane of the NS, due to the fact that the magnetic pressure is maximum at the equator. Therefore, if the magnetic field can be buried in this latitude, it will be buried in all latitudes of the NS.

The code developed by Romero et al. (2005) requires as input the knowledge of the density, velocity, thermal pressure, and magnetic pressure at both left and right states of the initial discontinuity. In all cases we consider, the left state corresponds to the force-free magnetosphere while the right state is occupied by the accreting fluid. To obtain the magnetic pressure of the left state, we find the solution of the Grad–Shafranov equation (see Section 5.1). This allows us to locate the position of the magnetopause where the Riemann problem must be solved. Since the inertia of the fluid at the magnetosphere can be neglected in front of the magnetic pressure, the value of the density on the left state is set to yield an Alfvén velocity near to one, the thermal pressure is set to be at least six orders of magnitude lower than the magnetic pressure, and the velocity is set to zero. On the other hand, the values on the right state are fixed to the corresponding values of density, pressure, and velocity of the stationary spherical accretion solution (see Section 3), and the magnetic pressure is set to zero.

A sketch of the different stages of the accretion process is shown in Fig. 5. The plots depict the location of the NS (including its core and inner and outer crust), the magnetosphere, the magnetopause, and part of the region where material is falling back. Each region is shaded in a different colour for a simple identification. Note that the scale ratio of the different regions is not preserved in the figure. The upper panel in Fig. 5 shows the initial state of the process. The panels on the left column show the expected evolution for a low magnetic field case (e.g. $B \lesssim 10^{13}$ G), while those on the right column correspond to a typical high magnetic field case (e.g. $B \gtrsim 10^{13}$ G). In general, the value of B separating between the two regimes depends on the accretion rate. For this figure, we have chosen a value of the magnetic field that corresponds to a representative example of our results (see Section 6), for which $\dot{M} = 10^{-5} M_\odot \text{ s}^{-1}$. At the beginning of the evolution, the reverse



Figure 5. Sketch of the representative stages of the accretion process. The upper panel shows the initial state of the process. The left column shows the expected evolutionary path for a low magnetic field ($B \lesssim 10^{13}$ G), while the right column corresponds to a typical high magnetic field case (e.g. $B \gtrsim 10^{13}$ G). A mass accretion rate of $10^{-5} M_{\odot} \text{ s}^{-1}$ is assumed. The scale ratio of the different regions is not preserved. See the main text for details.

shock falls over the magnetosphere. The magnetic field lines are confined inside the magnetosphere, which is shown in white on the diagram. Depending on the position of the sonic point, which in turn depends on the values of the specific entropy and the accretion rate, the motion of the reverse shock may be either supersonic or subsonic. We limit the qualitative description of the evolution below to the case of a supersonic reverse shock as in the subsonic case no accretion shock forms, as shown in Section 5.2.

The middle two panels in both evolutionary tracks show only qualitative differences in the size of the resulting magnetosphere after its compression and in the amplitude of the instabilities that may arise in the magnetopause (see below). Therefore, our description can be used for either path keeping this quantitative difference in mind. The evolution on the left column shows the case where the magnetic pressure is weak compared with the ram pressure of the fluid. In this case, the magnetosphere shrinks significantly until the equilibrium point is reached (R_{mp} ; zero speed contact discontinuity) close to the NS surface at $R_s \sim 10$ km. If the infall of the reverse shock is supersonic, an accretion shock will appear simultaneously. The location of this accretion shock is shown on the horizontal axis of the four middle panels. As a result, the velocity of the reverse shock is reduced due to the presence of a region of subsonic accretion behind the accretion shock. Nevertheless, as through the accretion shock the momentum is conserved, the compression is not affected. The evolution on the right column, where the magnetic pressure is stronger, is qualitatively similar, only the accretion shock is located further away from the NS surface and the magnetosphere is not so deeply compressed.

As we will discuss below in more detail, the compression phase is unstable against the growth of Rayleigh–Taylor instabilities and the development of convection on the dynamic time-scale. Therefore, the fluid and the magnetic field lines can mix, which provides a mechanism for the infalling fluid to actually reach the star. As the fluid reaches the NS, the mass of the star grows from M_s^* to M_s and its radius increases from R_s^* to R_s , encompassing the twisted magnetic field lines a short distance away. The mass accreted δM forms part of the new crust of the NS, whose final radius will depend on the total mass accreted during the process. The bottom panels of the diagram depict a magnified view of the NS to better visualize the rearrangement the mass of the star and the magnetic field undergo. If the radius R_{mp} of the equilibrium point is lower than the new radius R_s , all the magnetic field lines will be frozen inside the NS new crust, as shown in the bottom-left plot of Fig. 5 which corresponds to the end of the accretion process for a low magnetic field evolution. In contrast, if the magnetic field is high, as considered on the evolutionary path on the right, the equilibrium point R_{mp} is far from the surface of the NS. Although part of the infalling matter may still reach the star and form a new crust, the mechanism is not as efficient as in the low magnetic field case. This is depicted in the bottom-right panel of the figure.

In our approach, which we discuss in more detail in the section on results, we compare the distance obtained by the Riemann solver for the location of R_{mp} (zero speed in the contact discontinuity) with the increment of the radius of the NS, δR , due to the pile-up of the accreting matter. If the radial location of the equilibrium point R_{mp} is lower than δR (as in the bottom-left panel of Fig. 5), we conclude that the magnetic field is completely buried into the NS crust. In contrast, if $R_{\text{mp}} > \delta R$, our approach does not allow us to draw any conclusion. In this case, multidimensional magnetohydrodynamic (MHD) numerical simulations must be performed to obtain the final state of the magnetic field.

Table 2. Models considered in this study.

Model no	Composition	Entropy (k_B/nuc)	NS mass (M_\odot)	MF distribution
Reference	He + NSE	10	1.4	Loop current
1	He + NSE	100	1.4	Loop current
2	He + NSE	1000	1.4	Loop current
3	He + NSE	5000	1.4	Loop current
4	He	10	1.4	Loop current
5	He	100	1.4	Loop current
6	He	1000	1.4	Loop current
7	He	5000	1.4	Loop current
8	C + NSE	10	1.4	Loop current
9	C + NSE	100	1.4	Loop current
10	C + NSE	1000	1.4	Loop current
11	C + NSE	5000	1.4	Loop current
12	He	10	1.4	Dipole
13	He	1000	1.4	Dipole
14	He	10	1.2	Loop current
15	He	10	1.6	Loop current
16	He	10	1.8	Loop current
17	He	10	2.0	Loop current

6 RESULTS

We turn next to describe the main results of our study. In order to be as comprehensive as possible, we cover a large number of cases which are obtained from varying the physical parameters of the model, namely the composition and entropy of the accreting fluid, the mass of the NS, and the initial magnetic field distribution. For all possible combinations of these parameters, the outcome of the accretion process depends both on the magnetic field strength and on the mass accretion rate. This dependence is presented in the following sections in a series of representative figures. A summary of all the combinations considered and the description of the model parameters can be found in Table 2.

6.1 Reference model

We use as a reference model the one corresponding to an accreting fluid with $s = 10k_B/\text{nuc}$, and composed essentially of helium. The nuclear reactions to reach NSE are also allowed in this model. The mass of the NS is $1.4 M_\odot$ and the magnetic field is generated by a *loop current* in the NS. The results are shown in Fig. 6. The solid lines in this figure represent the distance of the equilibrium point δR (position of the magnetopause) above the NS surface as a function of the total accreted mass δM . The limit of the horizontal axis is given by the maximum mass that can be accreted without forming a black hole. Each line corresponds to a different value of the initial magnetic field, indicated in the legend of the figure. The yellow area represents the region in which the accretion of the reverse shock is supersonic and the black dotted line shows the limit of the accretion shock. The dashed red line shows the radial location of the new surface of the star due to the accretion of the infalling matter. The lines which cross the dashed red line have the equilibrium point inside the crust of the NS and, therefore, the corresponding magnetic fields will be buried into the crust. However, for the lines that are in the white area, the equilibrium point is not close enough to the NS surface and the magnetic field cannot be buried. Note that for initial values of the magnetic field $B \gtrsim 10^{15}$ G, the magnetic field is never buried for all mass accretion rates considered.

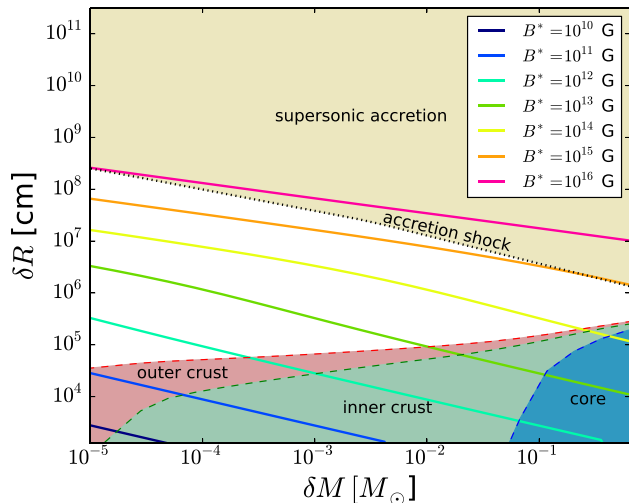


Figure 6. Distance above the star of the equilibrium point δR as a function of the total mass accreted δM for each value of the magnetic field (solid lines) for the reference model. The yellow area indicates the region where the accretion flow is supersonic. The dotted line represents the limit of the accretion shock. The red area marks the outer crust of the NS after accretion, while the green and blue areas display the inner crust and the core, respectively, as shown in Fig. 5.

An alternative view of this result is shown in Fig. 7. The goal of this representation is to provide a clearer representation of the dependence of the equilibrium point with the span of values of the magnetic field and the total mass accreted we are considering. The figure shows the isocontours where the equilibrium point is equal to the increment of the radius of the NS, i.e. $R_{\text{mp}} = \delta R$. The two lines plotted (dotted, $t = 10^4$ s, and solid, $t = 10^3$ s) correspond to the limits of the total accretion time, which relates the accretion rate \dot{M} and the total mass increment δM . The black area indicates the values of the maximum mass of the NS beyond

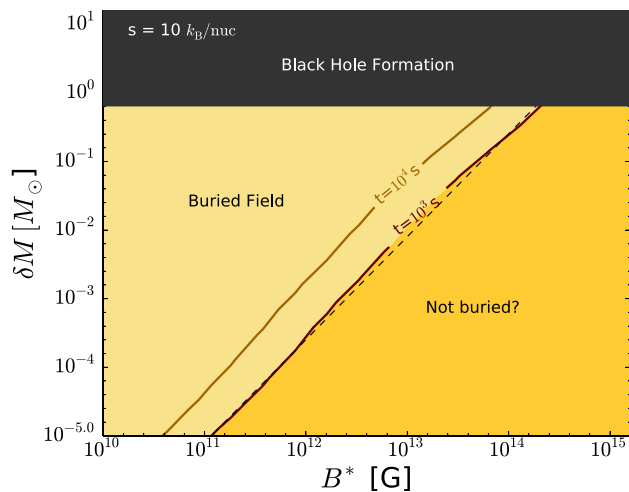


Figure 7. Outcome of the accretion depending on the total accreted mass (δM) and the initial magnetic field (B^*) for the reference model. For the two accretion times considered, $t = 10^3$ s (dark orange) and $t = 10^4$ s (light orange), the respective line splits the parameter space in a region where the magnetic field will be buried (left side) or not completely buried (right side). Above certain δM , a black hole will be formed. The dashed line represents the fit shown in equation (25).

which it will form a black hole. The dark orange region represents the span of values of δM and B^* where we cannot assure that the magnetic field could be buried completely. The light orange area, on the other hand, represents the cases where the magnetic field is totally buried. The results show that for low values of the magnetic field ($B^* < 10^{11}$ G) the field can be buried even with the lowest accretion rates we have considered. As expected, as the accreted mass increases, it is possible to bury the magnetic field for larger initial field values, up to a certain maximum. Indeed, for $B^* > 2 \times 10^{14}$ G, we cannot find any accretion rate which can bury the magnetic field.

6.2 Models with higher specific entropy

We turn next to analyse the behaviour of the magnetic field compression when the accreting fluid has higher specific entropy than in the reference model, keeping the same conditions for the composition, mass, and magnetic field distribution (models 1, 2, and 3 in Table 2). Fig. 8 shows the results for values of the specific entropy of $s = 100k_B/\text{nuc}$, $1000k_B/\text{nuc}$, and $5000k_B/\text{nuc}$ compared with the reference model ($s = 10k_B/\text{nuc}$). For the model with specific entropy $100k_B/\text{nuc}$, the results are very similar to the reference model as both lines almost perfectly overlap. For larger specific entropy, the difference is more noticeable; for $s = 1000k_B/\text{nuc}$ and $5000k_B/\text{nuc}$, the burial/re-emergence boundary of the parameter space is shifted towards larger magnetic fields, i.e. higher entropy material compress the magnetosphere more easily and it is possible to bury larger magnetic fields. This behaviour can be understood if one considers that the equilibrium point is a balance between the total pressure of the infall material, $p_{\text{tot}} = p + p_{\text{ram}} \approx p + \rho v^2$, and the magnetic pressure of the magnetosphere. For low specific entropy, the total pressure is dominated by the ram pressure and changes in s do not produce significant changes in the equilibrium point. Above a certain threshold, the thermal pressure p dominates the total pressure and increasing s induces a larger compression of the magnetosphere, shifting the equilibrium point downwards. For realistic values of the specific entropy in supernovae, $s \sim 10\text{--}100k_B/\text{nuc}$ (Kifonidis et al. 2003, 2006; Scheck et al. 2006), we expect the ram pressure to be dominant and hence the influence of s to be minimal. Even for an unrealistically large value of the specific entropy, $5000k_B/\text{nuc}$, the maximum magnetic field that can be buried increases one order of

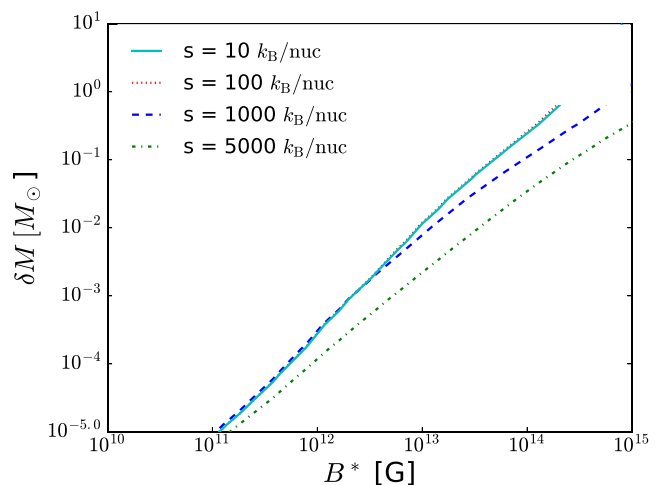


Figure 8. Similar to Fig. 7 but for the models with different specific entropy for the accreting fluid (namely, models 1 to 3 and reference). All cases are shown for a total accretion time of 10^3 s. Each line ends at the maximum mass of the corresponding model.

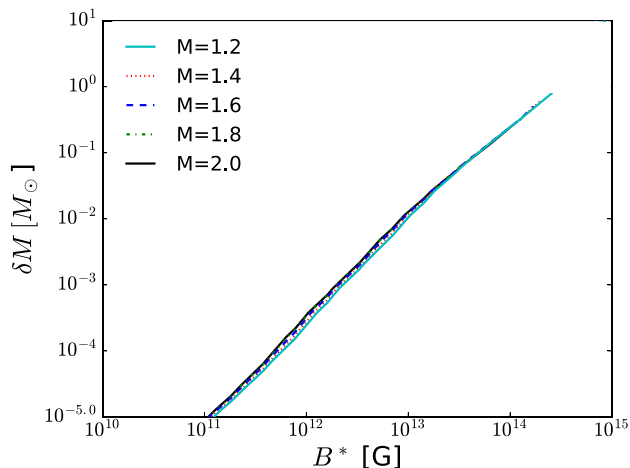


Figure 9. Similar to Fig. 7 for the models with different NS masses: 1.2, 1.6, 1.8, $2.0 M_{\odot}$ (models 14, 15, 16, and 17 and reference). All cases are shown for a total accretion time of 10^3 s. Each line ends at the maximum mass of the corresponding model.

magnitude at most, and only for the largest mass accretion rates considered.

6.3 Models with different NS masses

We consider next the effect of the NS mass, within astrophysically relevant limits. According to observations (see Lattimer 2012, and references therein), the lower limit for the NS mass is around $1.2 M_{\odot}$. The maximum achievable mass of an NS is strongly dependent on the EoS (Lattimer & Prakash 2005). Nowadays, there are a few observations that support the existence of pulsars and NSs with masses greater than $1.5 M_{\odot}$, in particular an observation of an $\sim 2 M_{\odot}$ NS (Demorest et al. 2010; Antoniadis et al. 2013). For this reason, we explore the results for several values of the NS mass between 1.2 and $2 M_{\odot}$. The results are shown in Fig. 9, where each line corresponds to a model with different NS mass as indicated in the legend. The results for all masses are very similar. In general, we observe that for more massive NSs, a higher accreted mass is needed to bury the magnetic field. Our interpretation is that higher mass NSs have lower radii and hence we have to compress more the magnetosphere to successfully bury it into the crust. Therefore, a higher accreted mass is needed to bury the field for NS with larger mass (smaller radius). Since the radius difference between a 1.2 and a $2 M_{\odot}$ NS is small, the impact of the NS mass on the burial is minimal. The maximum value of the magnetic field which can be buried is $\sim 2 \times 10^{14}$ G in all cases. For smaller NS masses, slightly larger values of the magnetic field can be buried due to the ability to support a larger accreted mass. We conclude that the burial of the magnetic field is not crucially sensitive to the NS mass.

6.4 Models with different EoSs

Fig. 10 shows the comparison of the results for the reference model when using the four different EoSs described in Section 4. For $M = 1.4 M_{\odot}$, the coordinate radius of these NS models is 12.25 km for APRDH, 12.11 km for APRNV, 15.77 km for LDH, and 15.37 km for LNV. Since the maximum mass is sensitive to the EoS, each line ends at different points in the δM versus B^* plot. The use of APRDH or APRNV EoSs leads to almost indistinguishable results (the two lines lay on top of each other). This is expected since the radius of

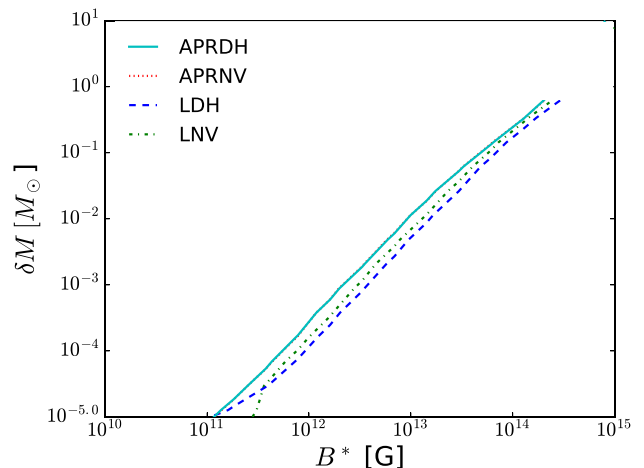


Figure 10. Similar to Fig. 7 for the models with different EoSs, an NS of mass $1.4 M_{\odot}$, and specific entropy of the accreting fluid $10 k_B/\text{nuc}$. All cases are shown for a total accretion time of 10^3 s. Each line ends at the maximum mass of the corresponding model.

these two models differs only by about 1 per cent, because the EoSs are very similar and only differ at low densities (at the crust). The LDH and LNV EoSs allow the burial of a larger magnetic field for a given accreted mass, in comparison with APRDH and APRNV. The maximum magnetic field that can be buried in the LDH and LNV models is $\sim 6 \times 10^{14}$ G and $\sim 5 \times 10^{14}$ G, respectively, which is about a factor of 2 larger than for the APRDH EoS. In general, for $M = 1.4 M_{\odot}$, EoSs resulting in a larger NS radius allow one to bury larger magnetic fields for a given δM . Given that the results of this work are meant to be an order-of-magnitude estimate of the location in the parameter space of the limit between burial and re-emergence, a difference of a factor of 2 due to the EoS does not change the main conclusions of this work. For practical purposes, the APRDH EoS can be taken as a good estimator for this limit.

6.5 Remaining models

We do not observe any significant differences with respect to the reference model in the results for the models with different initial composition of the reverse shock (models 8 to 11) or the ones using the NSE calculations (models 4 to 7). As a result, we do not present additional figures for these models since the limiting lines overlap with those of the reference model. The observed lack of dependence is due to the fact that the EoS only depends on the electron fraction, Y_e . This value is obtained from the ratio between the mean atomic mass number (\bar{A}) and the mean atomic number (\bar{Z}). For both cases of pure helium and pure carbon, this ratio is equal to $Y_e = 0.5$ and, consequently, the values of pressure and density for the accreting fluid are almost identical, producing differences in the results below the numerical error of our method.² In the case of the NSE calculation, the reason is similar. For low entropies ($s = 10, 100 k_B/\text{nuc}$), the temperature is not sufficiently high to start the nuclear reactions and the composition remains constant throughout the accretion phase. For higher entropies, although the value of the electron fraction may differ from 0.5 during the accretion process, the differences produced in the thermodynamical variables lead

² The numerical error is dominated by the calculation of the equilibrium point, which is computed with a relative accuracy of 10^{-4} .

to changes in the results of the Riemann problem still below the numerical error of the method.

Regarding the initial distribution of the magnetic field, we do not observe either any significant difference in the results in the two cases that we have considered, *loop current* and *dipole*. Given that we are comparing models with the same effective magnetic field, B^* , and thus the same magnetic dipolar moment, the magnetic field is virtually identical at long radial distances and the only differences appear close to the NS surface. In practice, the magnetic field structure only changes the details of the burial in the cases in which the equilibrium point is close to the burial depth (the limiting line plotted in Figs 7–10), but it does not change the location of the limit itself in a sensitive way. As a conclusion, we can say that the dominant ingredient affecting the burial of the magnetic field is the presence of a dipolar component of the magnetic field but, for order-of-magnitude estimations, a multipolar structure of the field is mostly irrelevant.

7 SUMMARY AND DISCUSSION

We have studied the process of submergence of magnetic field in a newly born NS during a hypercritical accretion stage in coincidence with core collapse supernova explosions. This is one of the possible scenarios proposed to explain the apparently low external dipolar field of CCOs. Our approach is based on 1D solutions of the relativistic Riemann problem, which provide the location of the spherical boundary (magnetopause) matching an external non-magnetized accretion solution with an internal magnetic field potential solution. For a given accretion rate and magnetic field strength, the magnetopause keeps moving inwards if the total (matter plus ram) pressure of the accreting fluid exceeds the magnetic pressure below the magnetopause. Exploring a wide range of accretion rates and field strengths, we have found the conditions for the magnetopause to reach the equilibrium point below the NS surface, which implies the burial of the magnetic field. Our study has considered several models with different specific entropy, composition, and NS masses. Assuming an accretion time of 1000 s, our findings can be summarized by a general condition, rather independent of the model details, relating the required total accreted mass to bury the magnetic field with the field strength. An approximate fit is (see the dashed line in Fig. 7)

$$\frac{\delta M}{M_{\odot}} \approx \left(\frac{B}{2.5 \times 10^{14}} \right)^{2/3}. \quad (25)$$

The most important caveat in our approach is that we are restricted to a simplistic 1D spherical geometry, which does not allow us to consistently account for the effect of different MHD instabilities that can modify the results. We also note that our scenario is quite different from the extensively studied case of X-ray binaries, in which the NS accretes matter from a companion but at much lower rates (sub-Eddington) and matter is mostly transparent to radiation during accretion. In that case, matter cools down through X-ray emission during the accretion process. Davidson & Ostriker (1973) and Lamb, Pethick & Pines (1973) already noticed this fact and predicted that the accretion will most likely be channelled through the magnetic poles, in analogy with the Earth’s magnetosphere. In the context of X-ray binaries, Arons & Lea (1976) and Michel (1977) were able to compute equilibrium solutions with a deformed magnetosphere and a cusp-like accretion region at the magnetic poles. However, as the same authors pointed out, these systems are unstable to the interchange instability (Kruskal & Schwarzschild 1954), a Rayleigh–Taylor-like instability in which magnetic field

flux tubes from the magnetosphere can rise, allowing the fluid to sink. This might allow for the formation of bubbles of material that fall through the magnetosphere down to the NS surface. In the case of a fluid deposited on top of a highly magnetized region, modes with any possible wavelength will be unstable (Kruskal & Schwarzschild 1954); however, in practice these instabilities are limited to the size of the magnetosphere ($\sim R_{\text{mp}}$) in the angular direction. As the bubbles of accreted material sink, magnetic flux tubes rise, as long as their magnetic pressure equilibrates the ram pressure of the unmagnetized accreting fluid (Arons & Lea 1976). Therefore, in a natural way, the equilibrium radius computed in Section 5.2 roughly determines the highest value at which the magnetic field can rise.

This accretion mechanism through instabilities has been shown to work in the case of X-ray binaries in global 3D numerical simulations (e.g. Kulkarni & Romanova 2008; Romanova et al. 2008). In the case of the hypercritical accretion present in the supernova fallback, Rayleigh–Taylor instabilities have been studied by Payne & Melatos (2004, 2007), Bernal et al. (2010), Bernal, Lee & Page (2013), and Mukherjee, Bhattacharya & Mignone (2013a,b). The simulations of Bernal et al. (2013) also show that the height of the unstable magnetic field over the NS surface decreases with increasing accretion rate, for fixed NS magnetic field strength, as expected. Using the method described in Section 5.2, we have estimated the equilibrium height over the NS surface for the four models presented in fig. 9 of Bernal et al. (2013), for their lower accretion rates ($\dot{M} \leq 10^{-6} M_{\odot} \text{ s}^{-1}$). Our results predict correctly the order of magnitude of the extent of the unstable magnetic field over the NS surface. Therefore, our simple 1D model for the equilibrium radius serves as a good estimator of the radius confining the magnetic field during the accretion process, although details about the magnetic field structure cannot be predicted. Another important difference with the binary scenario is the duration of the accretion process. In X-ray binaries, a low accretion rate is maintained over very long times, so that instabilities have always time to grow. In our case, hypercritical accretion can last only hundreds or thousands of seconds, and depending on the particular values of density and magnetic field, this may be too short for some instabilities to fully develop. This issue is out of the scope of this paper and deserves a more detailed study.

Our main conclusion is that a typical magnetic field of a few times 10^{12} G can in principle be buried by accreting only 10^{-3} – $10^{-2} M_{\odot}$, a relatively modest amount of mass. This estimate has interesting implications: since it is likely that most NSs can undergo such an accretion process, and the field would only re-emerge after a few thousand years (Geppert et al. 1999; Viganò & Pons 2012), the CCO scenario is actually not peculiar at all and we expect that most very young NSs show actually an anomalously low value of the magnetic field. In contrast, magnetar-like field strengths are much harder to screen and the required accreted mass is very large, in some cases so large that the NS would collapse to a black hole. We also stress that the concept of *burial* of the magnetic field refers only to the large-scale dipolar component, responsible for the magnetospheric torque spinning down the star. Small-scale structures produced by instabilities can exist in the vicinity of the star surface, and this locally strong field is likely to have a visible imprint in the star thermal spectrum, as in Kes 79 (Shabaltas & Lai 2012), without modifying the spin-down torque. However, the high-field burial scenario should not be very common because high-field NSs are only a fraction to the entire population, and only a part of them would undergo the fallback episode with the right amount of matter. This is consistent with the recent results of Bogdanov, Ng & Kaspi

(2014) who searched for the hidden population of evolved CCOs among a sample of normal pulsars with old characteristic ages but close to an SNR. None of the eight sources studied was found to have a luminosity higher than 10^{33} erg s⁻¹, which would have been evidence of a hidden strong field. They all show X-ray luminosities in the 0.3–3 keV band of the order of 10^{31} erg s⁻¹ (or similar upper limits), consistent with the properties of other low-field NSs with $B \approx 10^{12}$ G. Thus, these sample of sources are not likely to be linked to the family of descendants of Kes 79-like objects, but there is no contradiction with these being pulsars with re-emerged normal fields. Finally, we note that the slow re-emergence process on time-scales of kyr mimics the increase of the magnetic field strength, and it is therefore consistent with a value of the braking index smaller than 3 (Espinoza et al. 2011), which should be common for all young pulsars in this scenario.

ACKNOWLEDGEMENTS

It is a pleasure to thank J. M. Martí for many fruitful discussions. This work has been supported by the Spanish MINECO grants AYA2013-40979-P and AYA2013-42184-P and by the Generalitat Valenciana (PROMETEOII-2014-069).

REFERENCES

- Aguilera D., Pons J. A., Miralles J. A., 2008, *A&A*, 486, 255
 Akmal A., Pandharipande V. R., Ravenhall D. G., 1998, *Phys. Rev. C*, 58, 1804
 Anile A. M., 1989, *Relativistic Fluids and Magneto-Fluids: With Applications in Astrophysics and Plasma Physics*. Cambridge Univ. Press, Cambridge
 Antón L., Zanotti O., Miralles J. A., Martí J. M., Ibáñez J. M., Font J. A., Pons J. A., 2006, *ApJ*, 637, 296
 Antoniadis J. et al. 2013, *Science*, 340, 448
 Arons J., Lea S. M., 1976, *ApJ*, 207, 914
 Bernal C. G., Lee W. H., Page D., 2010, *Rev. Mex. Astron. Astrofis.*, 46, 309
 Bernal C. G., Lee W. H., Page D., 2013, *ApJ*, 770, 106
 Bignami G. F., Caraveo P. A., De Luca A., Mereghetti S., 2003, *Nature*, 423, 725
 Blondin J. M., 1986, *ApJ*, 308, 755
 Bogdanov S., Ng C.-Y., Kaspi V. M., 2014, *ApJ*, 792, L36
 Bonanno A., Urpin V., Belvedere G., 2005, *A&A*, 440, 199
 Burrows A., Lattimer J. M., 1986, *ApJ*, 307, 178
 Chevalier R. A., 1989, *ApJ*, 346, 847
 Colgate S. A., 1971, *ApJ*, 163, 221
 Davidson K., Ostriker J. P., 1973, *ApJ*, 179, 585
 De Luca A., Mereghetti S., Caraveo P. A., Moroni M., Mignani R. P., Bignami G. F., 2004, *A&A*, 418, 625
 Demorest P. B., Pennucci T., Ransom S. M., Roberts M. S. E., Hessels J. W. T., 2010, *Nature*, 467, 1081
 Douchin F., Haensel P., 2001, *A&A*, 380, 151
 Endeve E., Cardall C. Y., Budiardja R. D., Beck S. W., Bejood A., 2012, *ApJ*, 751, 26
 Espinoza C. M., Lyne A. G., Kramer M., Manchester R. N., Kaspi V. M., 2011, *ApJ*, 741, L13
 Faucher-Giguère C.-A., Kaspi V. M., 2006, *ApJ*, 643, 332
 Fryer C. L., 2006, *New Astron. Rev.*, 50, 492
 Gabler M., Cerdá-Durán P., Font J. A., Müller E., Stergioulas N., 2012, *MNRAS*, 430, 1811
 Geppert U., Page D., Zannias T., 1999, *A&A*, 345, 847
 Gotthelf E. V., Halpern J. P., 2007, *ApJ*, 664, L35
 Gotthelf E. V., Halpern J. P., Seward F. D., 2005, *ApJ*, 627, L390
 Gotthelf E. V., Halpern J. P., Alford J., 2013, *ApJ*, 765, 58
 Goussard J.-O., Haensel P., Zdunik J. L., 1998, *A&A*, 330, 1005
 Gullón M., Miralles J. A., Viganò D., Pons J. A., 2014, *MNRAS*, 443, 1891
 Halpern J. P., Gotthelf E. V., Camilo F., Seward F. D., 2007, *ApJ*, 665, 1304
 Halpern J. P., Gotthelf E. V., 2010, *ApJ*, 709, 436
 Hammer N. J., Janka H.-Th., Müller E., 2010, *ApJ*, 714, 1371
 Ho W. C. G., 2011, *MNRAS*, 414, 2567
 Houck J. C., Chevalier R. A., 1991, *ApJ*, 376, 234
 Hui C. Y., Becker W., 2006, *A&A*, 454, 543
 Jackson J. D., 1962, *Classical Electrodynamics*. Wiley, New York
 Janka H.-T., Langanke K., Marek A., Martínez-Pinedo G., Müller B., 2007, *Phys. Rep.*, 442, 38
 Jøgerst C. C., Almgren A., Woosley S. E., 2010, *ApJ*, 723, 353
 Kifonidis K., Plewa T., Janka H. Th., Müller E., 2003, *A&A*, 408, 621
 Kifonidis K., Plewa T., Scheck L., Janka H. Th., Müller E., 2006, *A&A*, 453, 661
 Kruskal M., Schwarzschild M., 1954, *Proc. R. Soc. Lond. A*, 223, 348
 Kulkarni A. K., Romanova M. M., 2008, *MNRAS*, 386, 673
 Lamb F. K., Pethick C. J., Pines D., 1973, *ApJ*, 184, 271
 Lattimer J., 2012, *Annu. Rev. Nucl. Part. Phys.*, 62, 485
 Lattimer J., Prakash M., 2005, *Phys. Rev. Lett.* 94, 111101
 Lichnerowicz A., 1967, *Relativistic Hydrodynamics and Magnetohydrodynamics*. Benjamin, New York
 Mereghetti S., De Luca A., Caraveo P. A., Becker W., Mignani R., Bignami G. F., 2002, *ApJ*, 581, 1280
 Michel F. C., 1972, *Ap&SS*, 15, 153
 Michel F. C., 1977, *ApJ*, 214, 261
 Mukherjee D., Bhattacharya D., Mignone A., 2013a, *ApJ*, 430, 1976
 Mukherjee D., Bhattacharya D., Mignone A., 2013b, *ApJ*, 435, 718
 Muslimov A., Page D., 1995, *ApJ*, 440, L77
 Negele J. W., Vautherin D., 1973, *Nucl. Phys. A*, 207, 298
 Obergaulinger M., Janka H. T., Aloy-Torás M. A., 2014, *MNRAS*, 445, 3169
 Page D., Lattimer J. M., Prakash M., Steiner A. W., 2004, *ApJS*, 155, 623
 Pandharipande V. R., Smith R. A., 1975, *Phys. Lett. B*, 59, 15
 Payne D. J. B., Melatos A., 2004, *ApJ*, 351, 569
 Payne D. J. B., Melatos A., 2007, *ApJ*, 376, 609
 Pons J. A., Geppert U., 2007, *A&A*, 470, 303
 Pons J. A., Reddy S., Prakash M., Lattimer J. M., Miralles J. A., 1999, *ApJ*, 513, 780
 Pons J. A., Miralles J. A., Geppert U., 2009, *A&A*, 496, 207
 Romanova M. M., Kulkarni A. K., Lovelace, Richard V. E., 2008, *ApJ*, 673, L171
 Romero R., Martí J. M., Pons J. A., Ibáñez J. M., Miralles J. A., 2005, *J. Fluid Mech.*, 544, 323
 Scheck L., Kifonidis K., Janka H.-Th., Müller E., 2006, *A&A*, 457, 963
 Seitzzahl I. R., Timmes F. X., Marin-Lafèche A., Brown E., Magkotsios G., Truran J., 2008, *ApJ*, 685, L129
 Seward F. D., Slane P. O., Smith R. K., Sun M., 2003, *ApJ*, 584, 414
 Shabaltas N., Lai D., 2012, *ApJ*, 748, 148
 Shapiro S. L., Teukolsky S. A., 2004, *Black Holes, White Dwarfs and Neutron Stars*. Wiley-VCH, Berlin
 Swartztrauber P. N., 1974, *SIAM J. Numer. Anal.*, 11, 1136
 Thompson C., Duncan R. C., 1993, *ApJ*, 408, 194
 Timmes F. X., 1999, *ApJS*, 124, 241
 Timmes F. X., Arnett D., 1999, *ApJS*, 125, 277
 Timmes F. X., Swesty D., 2000, *ApJS*, 126, 501
 Ugliano M., Janka H. T., Marek A., Arcones A., 2012, *ApJ*, 757, 69
 Viganò D., Pons J. A., 2012, *MNRAS*, 425, 2487
 Viganò D., Rea N., Pons J. A., Perna R., Aguilera D. N., Miralles J. A., 2013, *MNRAS*, 434, 123
 Wongwathanarat A., Müller E., Janka H.-Th., 2015, *A&A*, 577, A48
 Woosley S. E., Weaver T. A., 1995, *ApJS*, 101, 181
 Woosley S. E., Heger A., Weaver T. A., 2002, *Rev. Mod. Phys.*, 74, 1015
 Young E. J., Chanmugan G., 1995, *ApJ*, 442, L53
 Zavlin V. E., Pavlov G. G., Sanwal D., Trumper J., 2000, *ApJ*, 540, L25
 Zhang W., Woosley S. E., Heger A., 2008, *ApJ*, 679, 639

APPENDIX A: RIEMANN PROBLEM

For an ideal magneto-fluid, the energy-momentum tensor $T^{\mu\nu}$ and Maxwell dual tensor $F^{*\mu\nu}$ are

$$T^{\mu\nu} = \rho \hat{h} u^\mu u^\nu + g^{\mu\nu} \hat{p} - b^\mu b^\nu, \quad (\text{A1})$$

$$F^{*\mu\nu} = u^\mu b^\nu - u^\nu b^\mu, \quad (\text{A2})$$

where $\hat{h} = 1 + \varepsilon + p/\rho + b^2/\rho$ is the specific enthalpy including the contribution of the magnetic field and $\hat{p} = p + b^2/2$ is the total pressure. Moreover, b^μ stands for the magnetic field measured by a comoving observer [see Antón et al. (2006) for details and its relation with the magnetic field B^μ measured by a generic observer]. The conservation of these two quantities, jointly with the conservation of the density current, equation (7), leads to the equations of ideal relativistic MHD,

$$\nabla_\mu J^\mu = 0, \quad (\text{A3})$$

$$\nabla_\mu T^{\mu\nu} = 0, \quad (\text{A4})$$

$$\nabla_\mu F^{*\mu\nu} = 0. \quad (\text{A5})$$

In the particular configuration of our Riemann problem, $u^\mu = W(1, v^x, 0, v^z)$, $b^\mu = (0, 0, b, 0)$, so the term $\nabla_\mu b^\mu b^\nu$ in the conservation of the stress-energy tensor vanishes. Therefore, the conservation equations reduce to the purely hydrodynamical case.

The Riemann problem in this particular configuration is described in terms of three characteristics, one entropy wave and two fast magnetosonic waves. The initial problem with two states L (left) and R (right) breaks up into four states,

$$L \mathcal{W}_\leftarrow L_* \mathcal{C} R_* \mathcal{W}_\rightarrow R, \quad (\text{A6})$$

where \mathcal{W} indicates a fast magnetosonic shock wave or a rarefaction wave and \mathcal{C} indicates the contact discontinuity. Solving the Riemann problem entails finding the intermediate states (L_* , R_*) and the position of the waves, which are determined by the pressure \hat{p}_* and the flow velocity v_*^x . If $\hat{p} \leq \hat{p}_*$, the wave is a rarefaction wave (a self-similar continuous solution), otherwise the solution is a shock wave. In our case (see Romero et al. 2005), the ordinary differential equation that allows us to obtain the solution for a rarefaction wave is given by

$$\frac{dv^x}{1 - (v^x)^2} = \pm \frac{(1 + b^2/(\rho h c_s)) \sqrt{\hat{h} + \hat{\mathcal{A}}^2(1 - w^2)} dp}{\hat{h}^2 + \hat{\mathcal{A}}^2} \frac{1}{\rho w}, \quad (\text{A7})$$

where $\hat{\mathcal{A}} = \hat{h} W v^z$, $w = c_s^2 + v_A^2 - c_s^2 v_A^2$, $v_A = b^2/\rho \hat{h}$ is the Alfvén velocity, and $c_s = \sqrt{\frac{1}{\hat{h}} \frac{\partial p}{\partial \rho}}|_s$ is the sound speed. The integration of equation (A7) allows us to connect the states ahead (a) and behind (b) the rarefaction wave. Rarefaction waves conserve entropy; hence, all the thermodynamical variables and the differential of p must be calculated at the same entropy of the initial state. From this

equation, the normal velocity behind the rarefaction can be obtained directly,

$$v_b^x = \tanh \hat{\mathcal{C}}, \quad (\text{A8})$$

with

$$\hat{\mathcal{C}} = \frac{1}{2} \log \left(\frac{1 + v_a^x}{1 - v_a^x} \right) \pm \int_{\hat{p}_a}^{\hat{p}_b} \frac{(1 + b^2/(\rho h c_s)) \sqrt{\hat{h} + \hat{\mathcal{A}}^2(1 - w^2)} dp}{\hat{h}^2 + \hat{\mathcal{A}}^2} \frac{1}{\rho w}. \quad (\text{A9})$$

In the same way, the velocity inside the rarefaction can be obtained by replacing the thermal pressure p by the total pressure \hat{p} .

On the other hand, shock waves should fulfil the so-called Rankine–Hugoniot conditions (Lichnerowicz 1967; Anile 1989)

$$[\rho u^\mu] n_\mu = 0, \quad (\text{A10})$$

$$[T^{\mu\nu}] n_\nu = 0, \quad (\text{A11})$$

$$[F^{*\mu\nu}] n_\nu = 0, \quad (\text{A12})$$

where n_μ is the unit normal to a given surface and $[H] \equiv H_a - H_b$, being H_a and H_b the boundary values. The normal flow speed in the post-shock state, v_b^x , can be extracted from the Rankine–Hugoniot equations (see Romero et al. 2005, for a detailed discussion),

$$v_b^x = \left(\hat{h}_a W_a v_a^x + \frac{W_s(\hat{p}_b - \hat{p}_a)}{j} \right) \quad (\text{A13})$$

$$\times \left(\hat{h}_a W_a + (\hat{p}_b - \hat{p}_a) \left(\frac{W_s v_a^x}{j} + \frac{1}{\rho_a W_a} \right) \right)^{-1}, \quad (\text{A14})$$

where $W_s = \frac{1}{\sqrt{1 - v_s^2}}$ is the Lorentz factor of the shock,

$$v_s^\pm = \frac{\rho_a^2 W_a^2 v_a^x \pm |j| \sqrt{j^2 + \rho_a^2 W_a^2 (1 - v_a^x)^2}}{\rho_a^2 W_a^2 + j^2} \quad (\text{A15})$$

is the shock speed, and

$$j \equiv W_s \rho_a W_a (V_s - v_a^x) = W_s \rho_b W_b (V_s - v_b^x) \quad (\text{A16})$$

is an invariant derived directly from the Rankine–Hugoniot jump conditions. These expressions, together with the Lichnerowicz adiabat,

$$[\hat{h}^2] = \left(\frac{\hat{h}_b}{\rho_b} + \frac{\hat{h}_a}{\rho_a} \right), \quad (\text{A17})$$

allow us to calculate the shock wave solution.

This paper has been typeset from a $\text{\TeX}/\text{\LaTeX}$ file prepared by the author.